Progress in Photovoltaics: Research and Applications

WILEY

PROGRESS IN PHOTOVOLTAICS

RESEARCH ARTICLE OPEN ACCESS

Enabling EVA for TOPCon: How Glass Frit Composition Governs Resistance to Acetic Acid–Induced Corrosion

Jiexi Fu[1] | Wei Wu[2] | Yan Zhang[2] | Lin Lv[2] | Chao An[2] | Weiguang Yang[2] | Zhan Wang[3] | Jinshuai Song[3] | Xutao Wang[1] | Xinyuan Wu[1] | Bram Hoex[1]

[1]School of Photovoltaic and Renewable Energy Engineering, University of New South Wales, Sydney, Australia | [2]Jolywood (Taizhou) Solar Technology Co Ltd, Taizhou, Jiangsu, China | [3]Jolywood (Suzhou) Sunwat Co Ltd, Suzhou, Jiangsu, China

Correspondence: Lin Lv (lvl01@jolywood.cn) | Xinyuan Wu (xinyuan.wu@unsw.edu.au) | Bram Hoex (b.hoex@unsw.edu.au)

Received: 20 December 2025 | **Revised:** 29 April 2026 | **Accepted:** 5 May 2026

Keywords: damp-heat | degradation | ethylene vinyl acetate | laser-assisted firing | metallization | reliability | solar module | TOPCon

ABSTRACT

Laser-assisted firing (LAF) technologies, such as laser-enhanced contact optimization (LECO), have enabled the reliable application of low-Al Ag pastes for front-side metallization in tunnel oxide passivated contact (TOPCon) solar cells, opening a pathway to improved damp-heat (DH) stability and glass–backsheet (G-B) module designs. To further lower production costs, ethylene–vinyl acetate (EVA) and EVA/polyolefin/EVA (EPE) encapsulants are commonly employed; however, their long-term hydrolytic degradation produces acetic acid, which promotes metallization corrosion. In this work, we systematically investigate the impact of glass frit chemistry in two commercial low-Al content Ag front pastes on the cell- and module-level stability of LAF-processed TOPCon devices. Accelerated acetic-acid exposure tests reveal that a Ba- and Zn-modified glass frit (Paste B) exhibits markedly improved resistance to interfacial degradation compared with a Pb- and B-rich frit (Paste A), as evidenced by a maintained series resistance, contact resistivity and Ag–Si interfacial integrity. Microscopic and elemental analyses revealed that Ba enrichment in the glass frit markedly improves interfacial stability relative to Pb- and B-rich formulations. At the module level, DH85 (85°C/85% RH) testing of G–B TOPCon modules (front EPE/rear EVA) demonstrates that Paste B limits the relative power loss to 4%–5% after 1500 h, whereas Paste A leads to severe fill-factor-driven degradation resulting in a power loss over 25%. These results establish a direct correlation between glass frit composition, acetic-acid corrosion resistance and DH stability, highlighting glass network engineering as a key lever for designing robust, low-cost metallization systems for next-generation TOPCon modules.

1 | Introduction

By 2024, tunnel oxide passivated contact (TOPCon) became the leading cell architecture in mass production, a leadership expected to continue throughout this decade. However, the persistent overcapacity in the photovoltaic (PV) industry has driven a sharp decline in module prices, prompting manufacturers to prioritize low-cost production strategies. Although these strategies can effectively reduce manufacturing costs, many of them accelerate module degradation under environmental stress.

TOPCon technology has been shown to be particularly susceptible to degradation, including corrosion during damp-heat (DH), potential-induced degradation (PID) and ultraviolet-induced degradation (UVID), all of which can shorten module lifetime

and lower system energy yield [1, 2]. The implementation of lower cost bills of materials (BOMs), especially polymer encapsulants and backsheets replacing rear glass, further increases reliability risks under real-world operating conditions.

DH testing has consistently revealed pronounced performance losses in TOPCon modules, demonstrating high sensitivity to the combined effects of moisture and elevated temperature [3–5]. This imposes strict design constraints, particularly for glass–backsheet (G–B) configurations, as polymer backsheets allow greater moisture ingress than glass–glass (G–G) structures [4]. In earlier generations, the use of silver–aluminium (Ag/Al) paste could easily result in front-side contact corrosion under DH exposure [6, 7]. The emergence of laser-assisted firing (LAF) techniques, such as laser-enhanced contact optimization (LECO), improved contact formation and open-circuit voltage (V_{oc}), resulting in higher cell and module efficiencies [8–10]. Furthermore, LAF enabled the adoption of low-Al Ag pastes in mass production, enhancing both cell- and module-level DH reliability and facilitating the use of backsheet-based module designs [7, 11].

To further reduce costs, polyolefin elastomer (POE) encapsulants are often replaced with ethylene–vinyl acetate (EVA). However, EVA undergoes thermo-oxidative and hydrolytic degradation, producing acetic acid as a by-product of vinyl acetate hydrolysis during long-term operation [12, 13]. Acetic acid is highly corrosive to metallization, leading to contact failure and power loss, making EVA less suitable for Ag/Al-based TOPCon modules [7, 14, 15]. In our previous work, we observed an ~6.2% relative power loss in low-Al Ag paste TOPCon modules after 1000 h of damp-heat DH85 (85°C/85% relative humidity [RH]) testing with G–B EVA encapsulation, significantly lower than the ~37% relative power loss observed in Ag/Al paste TOPCon modules under identical conditions [7].

Nevertheless, as the industry demands higher reliability of modules with low-cost BOMs under DH85 conditions, further advancements in materials and process optimization are needed to alleviate DH-induced degradation in TOPCon modules. Given that low-Al Ag pastes have only recently been adopted in conjunction with LAF processes for TOPCon technology, limited studies have systematically assessed the long-term stability of different low-Al Ag pastes, and the underlying mechanisms governing their cell-to-module reliability remain insufficiently understood.

Following the acetic-acid exposure approaches reported by Iqbal et al. [14] and ChenLi et al. [2], this work employs controlled acid soaking tests to investigate corrosion-induced degradation in TOPCon solar cells. Although previous studies mainly focused on cell-level degradation, the translation of acetic-acid-induced metallization corrosion to module-level reliability, particularly for LAF-processed TOPCon cells, remains insufficiently addressed. Here, we extend these established methodologies by correlating cell-level acid degradation with long-term module performance under DH85 conditions through a combined analysis of acid soaking, electrical characterization, detailed compositional and interfacial characterization, and 1500-h DH85 testing of laminated minimodules. Overall, this study establishes a direct correlation between glass-frit composition, corrosion resistance and metallization reliability, providing valuable guidance for the design of acid-resistant Ag pastes for next-generation, low-cost TOPCon modules.

2 | Experimental Details

The experimental workflow is presented in Figure 1a. Reliability assessments were performed at both the cell and module level, with electrical characterization conducted throughout the aging tests to monitor parameter evolution. Elemental analysis was carried out on selected regions (tokens/stripes) obtained from the same batch or from aged samples to identify compositional changes. Two types of low-Al Ag paste TOPCon solar cells fabricated by our industry partner were used in this study. Regarding

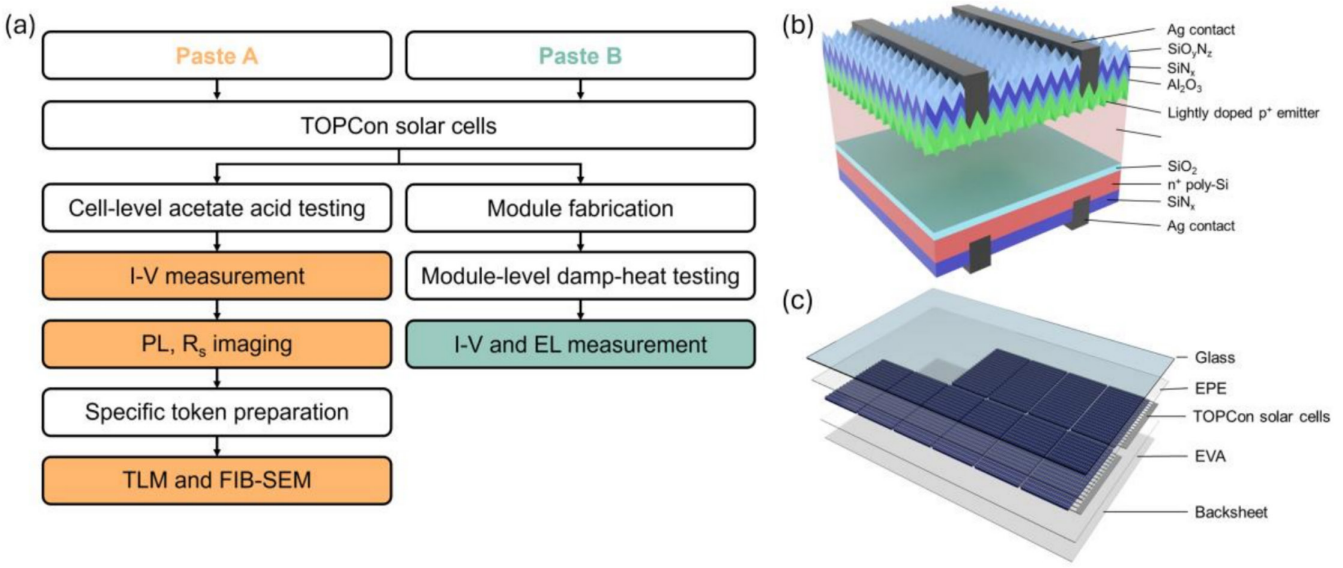

FIGURE 1 | (a) Experimental workflow for module accelerated damp-heat testing, (b) schematic representation of the TOPCon solar cells and (c) glass–backsheet (G–B) TOPCon modules utilized in this study.

the LECO process, the cells were processed using the industrial settings provided by the manufacturer. The key LECO parameters used for the cells in this study were power supply voltage of approximately 16 V, power supply current corresponding to the industrial setting, total laser power of approximately 70 W, laser wavelength of 1030 nm and laser frequency of 1000 Hz. All TOPCon cells were manufactured on G10 n-type Czochralski (Cz) silicon (Si) wafers (182 mm × 183.75 mm), with four samples prepared for each condition. The cell architecture is shown in Figure 1b. The front surface comprises a lightly boron-doped p^+ emitter (~300 Ω/□) passivated by an aluminum oxide/silicon nitride/silicon oxynitride ($Al_2O_3/SiN_x/SiO_yN_z$) stack, whereas the rear side consists of a silicon oxide (SiO_2) tunneling layer, a phosphorus-doped polycrystalline silicon layer and a SiN_x passivation layer. Following screen printing, all cells were fired and subsequently subjected to a LAF process to form ohmic contacts. The key distinction between the two cell types was their front-contact metallization, referred to as Pastes A and B. The paste composition differences were analyzed by inductively coupled plasma mass spectrometry (ICP-MS) (NexION 5000, PerkinElmer, United States). The paste samples were first digested prior to ICP analysis. For accurate Ag quantification, nitric acid (HNO_3) digestion was employed rather than hydrochloric acid (HCl) to avoid precipitation or complexation of Ag in chloride-containing media. Ag was quantified by ICP-OES, whereas the other elements were analysed by ICP-MS after subsequent mixed-acid digestion. To ensure a fair comparison, the same Ag rear paste was used for all samples.

All TOPCon cells were thoroughly cleaned to eliminate potential contaminants introduced during transportation and then placed in cassettes and immersed in sealed containers of 0.10 mol/L acetic acid at room temperature (25°C). This concentration was selected to reproduce the acidic conditions arising from EVA degradation in fielded modules, where in situ acetic acid accumulation has been reported to lower the local pH to values between ~2 and 5, depending on the backsheet permeability [16, 17]. The acetic acid solution was not refreshed throughout the experiment, and its volume was sufficiently large to ensure that any change in concentration during exposure remained negligible.

Before and after each exposure, the current–voltage (I–V) characteristics were measured using a pv-tools LOANA system. The I–V parameters were normalized to a reference cell measured simultaneously. The normalized value was defined as S/R, where S and R represent the sample and reference values, respectively, and the relative change between two measurements was calculated as (S2/R2) / (S1/R1) − 1. The photoluminescence (PL) and series resistance (R_s) mappings were obtained using a BT Imaging R3 tool. In addition, contact resistivity (ρ_c) was evaluated using the transfer length method (TLM). Strips with a width of 6 mm were prepared from both Pastes A and B samples and immersed in a 0.10 mol/L acetic acid solution for 10 min. Eight stripes (four front-side and four rear-side) were used for each paste type. Contact resistivity values were recorded before and after acid treatment.

To further investigate chemical and microstructural changes, the Ag pastes were analyzed by ICP-MS, and cross-sections of the corroded Ag fingers were prepared by focused ion beam (FIB) milling and imaged using a Zeiss Crossbeam 550. Scanning electron microscope (SEM) imaging at an accelerating voltage of 15 kV enabled visualization of voids, glass-phase evolution and disruption of the Ag–Si contact interface. During FIB operation, the sample stage was tilted 54° relative to the ion beam and 36° relative to the sample surface, with image scaling corrected accordingly. Energy-dispersive spectroscopy (EDS) was performed under the same SEM conditions using an Oxford Instruments Ultim Max detector, and the spectra were processed in AZtec software to obtain quantitative elemental ratios and spatial distributions [18]. Initial cross-sectional EDS mappings of both pastes are shown in Figure S2. The point ID function was used to perform relative elemental quantification.

The damp-heat testing workflow, outlined in Figure 1a, involved periodic I–V characterization and electroluminescence (EL) imaging of all modules. Accelerated aging was performed under damp-heat (DH85, 85°C/85% RH) conditions following the IEC 61215 standard [19]. Module fabrication followed the glass/EPE/TOPCon/EVA/backsheet structure shown in Figure 1c. Three modules per paste type were laminated for DH85 testing. Electrical performance measurements were obtained using a GIV-200DS2616 flash tester (Gsolar Power). After 1500 h of DH85 exposure, I–V and EL measurements were repeated to identify degradation patterns and quantify performance losses.

3 | Results and Discussion

3.1 | Cell-Level Acetic Acid Testing on LAF TOPCon Solar Cells

Both samples exhibited similar initial I–V characteristics, with efficiencies of approximately 25.2%, fill factors (FF) around 84.5%, short-circuit current densities (J_{sc}) of about 40.8 mA/cm^2, V_{oc} of around 734 mV and $R_s \sim 0.4\,\Omega\cdot cm^2$. Figure 2a–e shows the time-dependent I–V data under acetic acid exposure, highlighting the distinctly different degradation rates of Pastes A and B. For cells fabricated with Paste A, the decline was rapid and catastrophic, with the relative efficiency decreasing by approximately 80%–90% within 120 min. This sharp drop is accompanied by a severe reduction in FF and a dramatic rise in R_s. The more than four-order-of-magnitude increase in R_s directly suppresses the fill factor, and the reduction in short-circuit current density is attributed to incomplete photocurrent collection caused by the extremely high series resistance rather than EQE changes. As the contact becomes heavily corroded and the local resistance increases, a substantial fraction of the generated current can no longer be extracted through the metal fingers, leading to the observed J_{sc} drop. At the same time, the slight decrease in V_{oc} (< 3%) can be explained by corrosion-induced damage at the Ag–Si contact, which creates additional recombination sites and initiates early interfacial failure. Although the open-circuit voltage decreases by only a small amount, it occurs earlier than in Paste B cells, indicating that interfacial failure initiates at an earlier stage. The premature and severe degradation of Paste A makes long-term monitoring impractical, as devices become unmeasurable after 2 h. In contrast, Paste B exhibits a more gradual degradation trend, with the efficiency loss remaining relatively slow over the 240-min exposure period. Although the

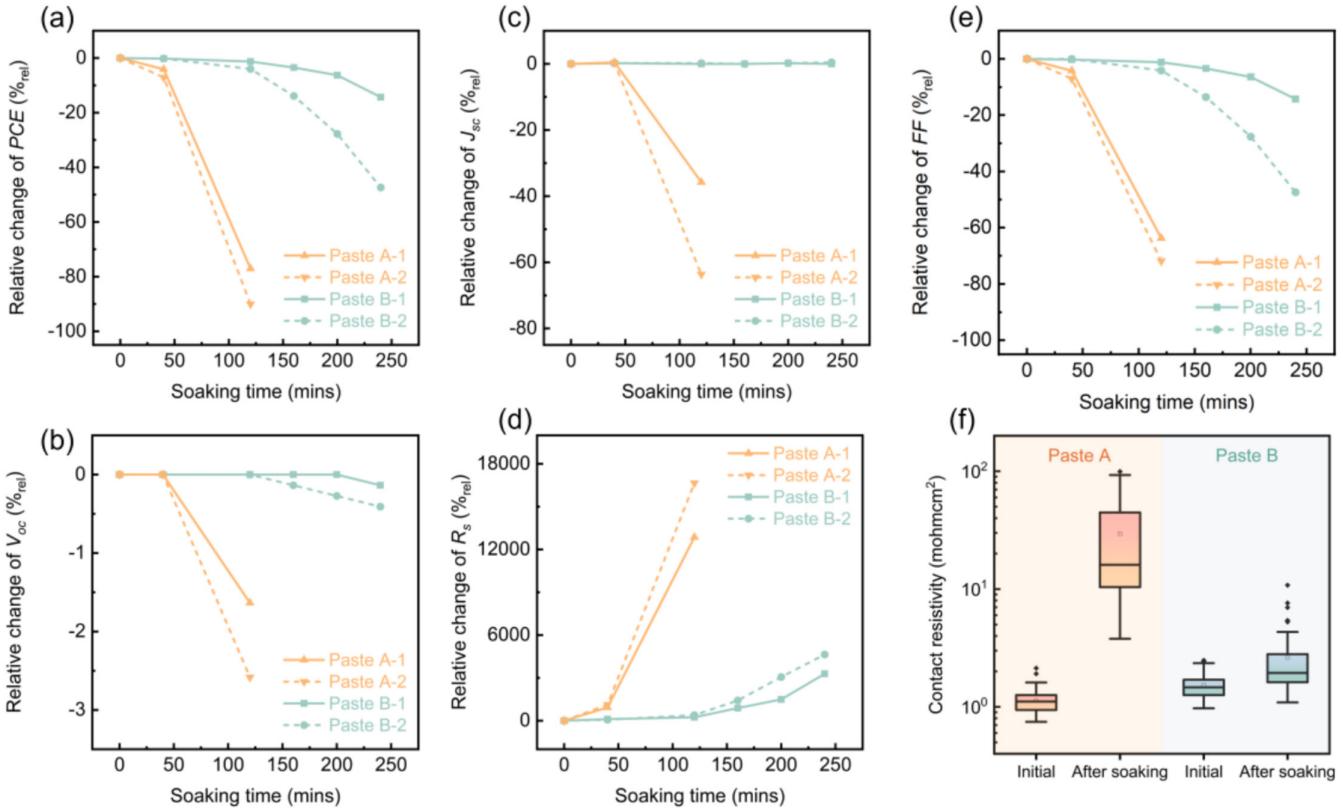

FIGURE 2 | Relative variations in (a) PCE, (b) V_{oc}, (c) J_{sc}, (d) R_s and (e) FF as a function of acetic acid aging time and (f) contact resistivity of Pastes A and B TOPCon strips measured before and after acetic acid exposure.

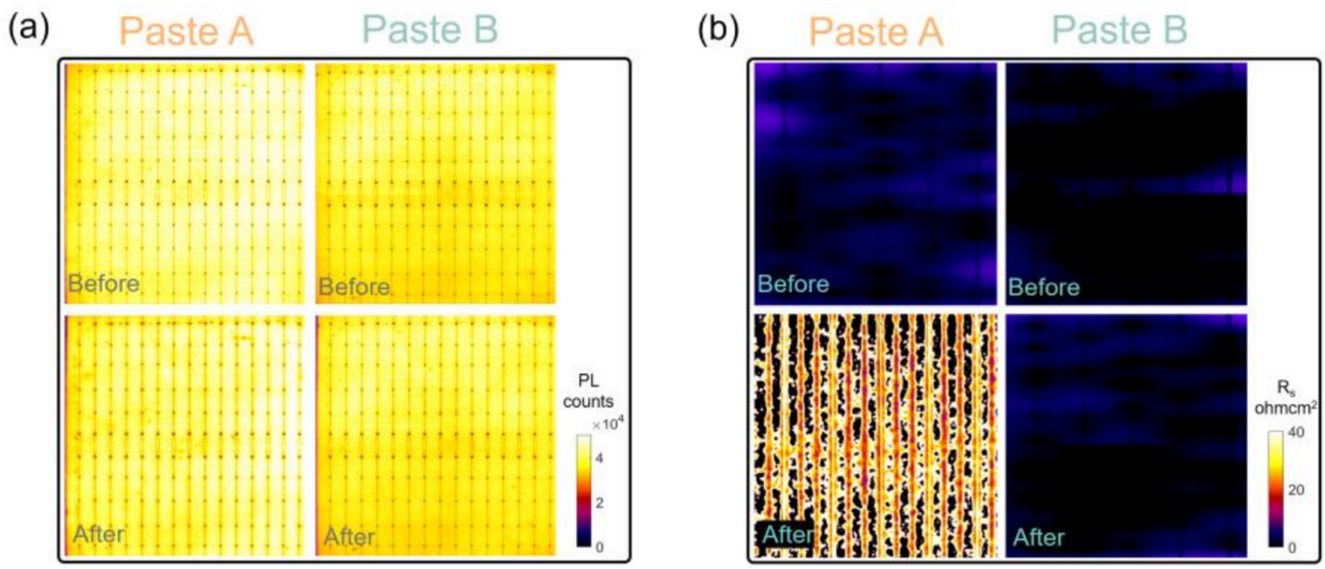

FIGURE 3 | (a) PL images of Pastes A and B TOPCon solar cells before and after acetic acid aging and (b) R_s images of Pastes A and B TOPCon solar cells before and after acetic acid ageing.

R_s shows a noticeable increase after 240 min of exposure, the rise remains moderate and does not reach the severe level observed in Paste A. Notably, both the V_{oc} and J_{sc} remain largely unchanged, suggesting that the corrosion of the interfacial frit progresses considerably more slowly than in Paste A. These findings demonstrate Paste B's superior corrosion resistance under acetic acid exposure.

The R_s mapping images shown in Figure 3b further validated these trends. After 80 min, Paste A cells exhibit large areas of elevated R_s, manifested as continuous finger-shaped high-resistance bands and fragmented hotspots, which are hallmarks of severe metallization corrosion and disrupted Ag–Si contacts. By contrast, Paste B retains an essentially uniform low-resistance distribution under identical conditions, indicating

that electrical continuity of the metal grid is largely preserved. In addition, the PL images exhibit only minor changes, consistent with the limited variation reported in Figure 2b.

Figure 2f shows the evolution of front ρ_c for Pastes A and B during the acetic acid aging test. Both samples exhibited low initial resistivity values, differing only slightly, with the Paste B sample showing slightly higher resistivity. After exposure, Paste A exhibited a sharp increase in ρ_c, with median values exceeding 40 mΩ·cm^2 and a broad distribution range. This wide variation indicates nonuniform corrosion, consistent with the irregular high-R_s regions observed in the front-side R_s mapping. Paste B displayed a distinctly different behaviour: After soaking, both the front and rear contacts maintained low ρ_c values, with only a slight increase (< 5 mΩ·cm^2) on the front side. The narrow post-soaking distribution suggests stable interfacial bonding and minimal glass corrosion. It is noted that the rear-side contacts were also measured before and after the ageing testing, and rear contact of all the cells retained a low resistivity (< 2 mΩ·cm^2). On the rear side, both samples maintained low and stable resistivity levels throughout the measurements.

3.2 | Paste Elemental Analysis

Table S2 summarizes the detailed ICP-MS results, and Figure 4a presents the relative elemental compositions of the two pastes in their initial state. Overall, both pastes consist of Ag as the main conductive phase, with boron (B), lead (Pb), barium (Ba), zinc (Zn), aluminium (Al), sodium (Na) and magnesium (Mg) forming the glass phase. The major compositional difference lies in the distribution of B and Ba: Paste A contains a higher amount of B but no Ba, whereas Paste B has a significant amount of Ba and less B. B is present in the frit mainly as B_2O_3, which acts as a glass-forming component and helps lower the softening temperature and viscosity of the frit, thereby facilitating frit flow and interfacial reaction during firing [20]. However, a more borate-dominated Pb/B glass network is also generally more vulnerable to hydrolysis and ion leaching in acidic environments unless stabilized by additional modifiers [21, 22]. Minor variations were also observed in Bi, Zn, Mg and Na contents. Pb- and B-rich phases are known to degrade readily in weakly acidic environments such as acetic acid, thereby accelerating corrosion at the Ag–Si contact interface [21, 23]. Zn is also likely to contribute to the behaviour of Paste B by modifying the interfacial glass structure and contact formation. However, based on

(a)

Element analysis by ICP-MS	Paste A	Paste B
Ag	97.9%	97.6%
Al	0.08%	0.09%
B	0.7%	0.2%
Ba	0.0%	0.7%
Bi	0.0%	0.001%
Pb	1.4%	1.2%
Fe	0.002%	0.002%
Mg	0.004%	0.0%
Na	0.002%	0.002%
Zn	0.0%	0.1%

(b)

Average elemental weight ratios (glass phase region)				
Element analysis by EDS	Paste A		Paste B	
	Initial	Acid aging	Initial	Acid aging
Ag	60.03%	96.79%	75.22%	94.43%
Al	2.85%	0.64%	0.38%	0.59%
Ba	0.24%	0.19%	8.35%	0.20%
Bi	0.86%	0.08%	0.17%	0.14%
Pb	34.02%	1.93%	11.48%	3.62%
Fe	0.12%	0.16%	0.06%	0.07%
Mg	0.03%	0.00%	0.02%	0.02%
Na	0.05%	0.02%	0.12%	0.00%
Zn	1.80%	0.18%	4.21%	0.93%

(c)

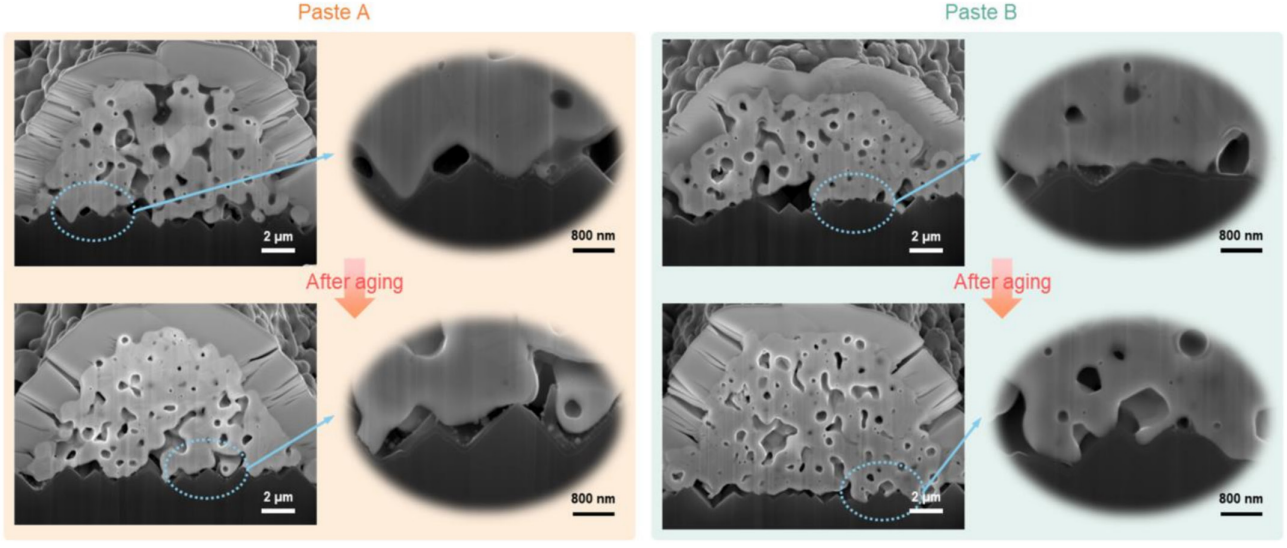

FIGURE 4 | (a) Relative elemental weight percentage of Paste A and B as obtained by ICP-MS, (b) relative elemental weight percentage ratios of the Ag contact region for solar cells fabricated using Paste A and B as obtained by EDS (excluding boron and silicon, see discussion in Section 3.1), (c) FIB-SEM cross-sectional images of fresh and degraded samples with Paste A and B.

prior studies, the role of ZnO in high-temperature Ag pastes is composition dependent: It may improve FF and assist interfacial densification in some frit systems, while also affecting the glass-phase conductivity and the erosion behaviour toward Si [24–27]. Therefore, in the present work, the improved stability of Paste B is attributed to the combined effect of the Ba/Zn-modified frit chemistry rather than to Zn alone. Na_2O and MgO act as network modifiers that help reduce the melting temperature and improve the glass fluidity. Previous studies have reported that incorporating Al_2O_3 and Fe_2O_3 into glass frits can strengthen the silicate framework and suppress ionic leaching under acetic conditions, thereby markedly enhancing the acid resistance of Ag metallization [28–31]. However, in Paste A, Fe is only present in trace amounts compared to Pb and B, and thus, the Pb–B system dominates the glass chemistry. In this work, the poorer corrosion resistance of Paste A is therefore attributed not simply to its higher B content but to the combined effect of its Pb/B-rich frit chemistry, which is more susceptible to acetic-acid-induced dissolution than the lower-B, Ba/Zn-modified frit in Paste B.

Figure 4b summarizes the averaged relative elemental weight percentage ratios obtained from EDS analyses on multiple points across the glass phase regions of the finger cross-sections, reflecting the compositional changes before and after acetic acid aging. The corresponding point locations are shown in Figure S1. For each sample, one bulk glass frit region and one interface glass frit region (each approximately $2\times3\,\mu m$) were measured, and about five EDS points were collected within each region. Because EDS analysis of light elements such as B is highly uncertain due to their low X-ray emission energy and strong absorption in the detector window and the Si signal may be affected by the substrate, both elements were excluded from the analysis [32, 33]. After excluding B and Si, the remaining elemental ratios were renormalized. The results show a significant reduction in the glass phase in both pastes after aging, indicating that the glass network dissolved and ions leached in the acidic environment, with Paste A exhibiting more severe degradation. Specifically, the Pb content in Paste A decreased from 34.02% to 1.93%, whereas in Paste B, it was reduced from 11.48% to 3.62%, suggesting that Paste B retained more of the glass composition.

The element most likely responsible for protecting the glass composition in Paste B appears to be Ba. From a chemical-bonding perspective, Ba^{2+} possesses a high ionic field strength and low polarizability, enabling the formation of strong ionic bonds with nonbridging oxygens (NBOs), which suppresses the attack of these oxygens by protons in the acidic medium [34, 35]. NBOs are oxygen ions bonded to only one network-forming atom (such as Si or B), carrying localized negative charges that serve as preferential sites for protonation or hydrolysis. Ba^{2+}, with its strong electrostatic field, can form stable ionic coordination with such O^{2-} species, reducing their polarizability and proton affinity. Although the introduction of BaO may increase the number of NBOs, the strong Ba–O bonding enhances the overall network stability under acidic conditions. In addition, some reports have shown that Ba^{2+} can improve the fluidity of conductive pastes [36, 37]. Therefore, Paste B may exhibit better flow behaviour than Paste A. Consistent with this, cross-sectional interface morphology shows that the interfacial glass in Paste B is uniform and thin, whereas Paste A exhibits local glass agglomeration [38, 39]. Consequently, after acetic acid soaking, Paste A developed larger interfacial gaps, whereas Paste B maintained continuous electrical contact at the interface. In addition, the presence of Bi exclusively in Paste B may also be beneficial, as previous studies on Bi_2O_3-containing glasses have shown that bismuth oxide can modify the glass network structure and improve resistance to dissolution in acidic environments. This enhancement is attributed to the ability of Bi_2O_3 to lower the glass softening temperature and increase its flowability and wetting on metallic surfaces, enabling the molten glass to more effectively fill interfacial voids during firing and form a denser and more continuous barrier against acid penetration [40–43].

Figure 4c shows the cross-sectional SEM of Ag fingers before and after immersion in acetic acid solution, which further shows the degradation process. The two pastes exhibit distinctly different degradation behaviours. At the initial state, both samples display the typical sintered-silver microstructure, consisting of a porous Ag bulk and a continuous glass interlayer at the Ag/Si interface. After immersion in acetic acid, Paste A shows severe interfacial delamination and extensive corrosion of the glass frit. The interfacial glass layer is almost completely dissolved, leaving exposed Ag particles and visible gaps between Ag and Si, which likely leads to electrical failure and accounts for the sharp increases in ρ_c and R_s observed macroscopically. In contrast, the Ag phase remains largely intact, suggesting that the primary degradation mechanism arises from dissolution of the Pb/B-rich glass rather than from metallic corrosion. In comparison, Paste B maintains a largely intact and well-adhered interface. Although partial corrosion of the glass phase within the finger bulk can be observed, the Ag/Si contact remains continuous without voids caused by frit dissolution.

3.3 | Module Damp-Heat Testing

Figure 5 presents the electrical performance parameters and EL images of modules fabricated with Pastes A and B after 1500 h of damp-heat exposure at 85°C and 85% relative humidity. Initially, both module types demonstrated comparable performance, with a maximum power (P_{max}) of approximately 581–582 W, a short-circuit current (I_{sc}) of about 13.7 A and a V_{oc} of roughly 52.8 V. The similarity of the initial parameters indicates that both paste formulations provided adequate contact formation and metallization quality immediately after fabrication. However, after the DH test, there were significant differences between the two modules. As shown in Figure 5b, the modules fabricated with Paste A exhibited approximately 28%–30% power degradation, which was dominated by a comparable reduction in FF, whereas I_{sc} and V_{oc} remained nearly unchanged. The reduction in FF is very likely due to an increase in R_s, consistent with the significant deterioration of Ag–Si contact integrity observed at the cell level after acetic acid soaking. The difference of J_{sc} between the cell-level acid-soaking behaviour and the module-level DH response mainly arises from the distinct degradation configurations. In the acetic-acid soaking test, the front metallization of bare cells is directly exposed to the acidic medium, which can rapidly disrupt local current-collection pathways and lead not only to severe FF loss, but also to an apparent decrease in J_{sc} when the front-grid transport becomes strongly limited. In contrast, within a laminated module, degradation tends to initiate preferentially near the ribbon/busbar regions. This is because

(a)

Sample	Paste A		Paste B	
	Module 1	Module 2	Module 1	Module 2
P_{max} (W)	581.70	581.10	581.30	582.70
I_{sc} (A)	13.73	13.73	13.75	13.77
V_{oc} (V)	52.75	52.75	52.75	52.79
I_{Pmax} (A)	13.03	13.01	12.97	13.00
V_{Pmax} (V)	44.65	44.68	44.81	44.84
FF (%)	80.34	80.26	80.15	80.19

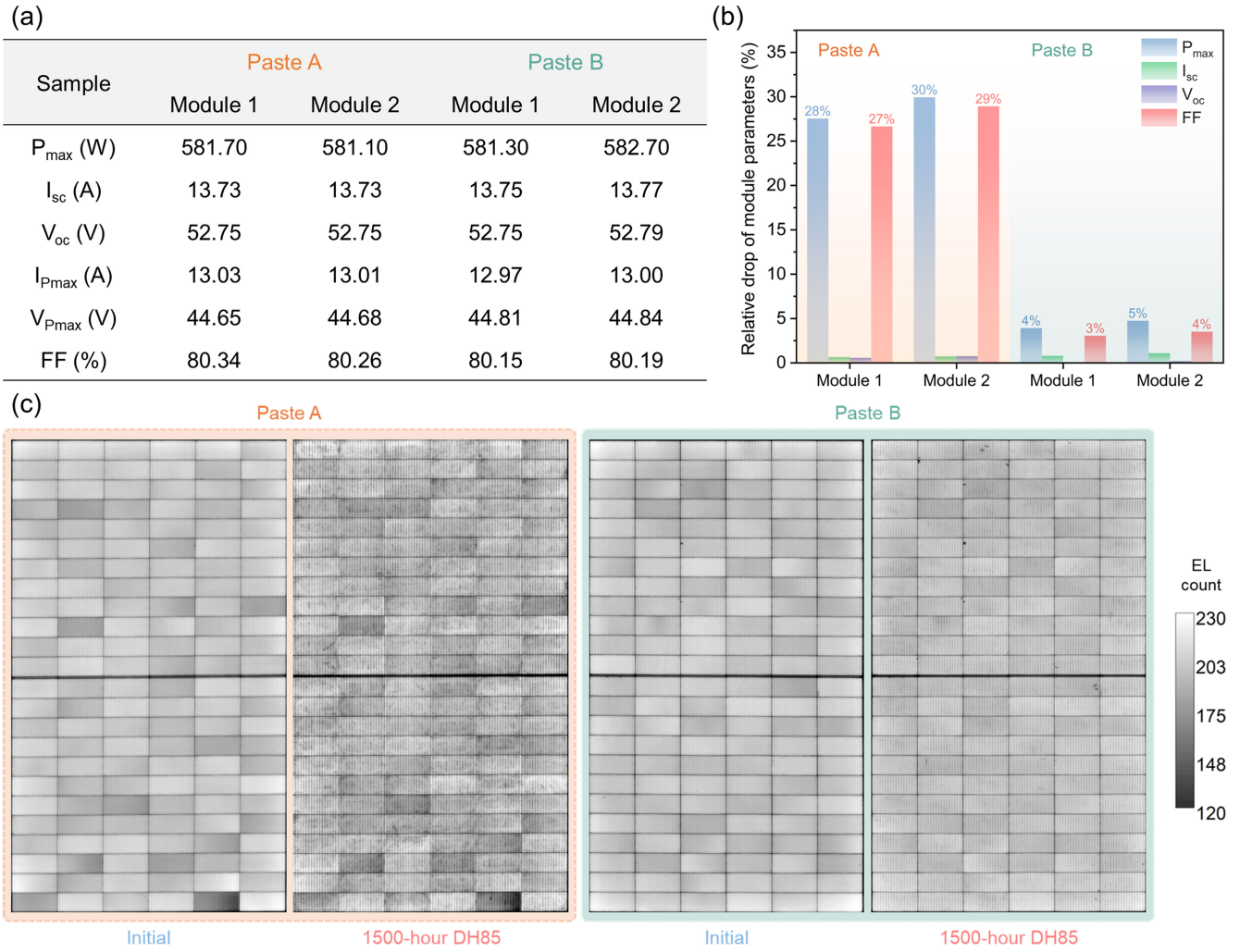

FIGURE 5 | Module-level DH85 (85°C/85% RH, 1500 h) reliability of TOPCon modules metallized with Pastes A and B. (a) Initial I–V characteristics of the modules, (b) relative power degradation after DH85 exposure and (c) EL images of the modules before and after 1500 h of DH85 testing.

the presence of the ribbon creates a relatively larger gap between the solar cell surface and the encapsulant, facilitating moisture ingress and transport to the cell surface. As a result, degradation is often observed along the ribbon/busbar areas. Furthermore, due to encapsulation and the interconnection architecture, degradation progresses more gradually at the module level. In this case, corrosion primarily increases series resistance, which is first reflected as FF loss. Meanwhile, the junction quality and optical properties remain largely unaffected in the early stages, resulting in relatively stable J_{sc} and V_{oc}. In contrast, the modules fabricated with Paste B maintained a relatively stable electrical output after the DH exposure, with P_{max} decreasing by only 4%–5%. Both I_{sc} and V_{oc} remained nearly constant, indicating that the cells' optical and recombination properties were unaffected. The slight decrease in FF can be attributed to minor transport-related losses, whereas the stable V_{oc} and I_{sc} indicate that junction and interfacial contact integrity were preserved. Relative to our earlier findings showing a 6.2% power loss after 1000 h of damp-heat exposure, the present results demonstrate a measurable enhancement in stability [7].

The EL imaging results further support these findings at the module level. For the Paste A modules, the post-DH images exhibit extensive darkening concentrated around busbar-connected grid regions, with darkened features extending along adjacent fingers, indicating resistive losses. The pronounced contrast variation among individual cells confirms that contact degradation was nonuniform, with the most corroded grid segments dominating. Such inhomogeneous degradation is consistent with the dispersed ρ_c distribution obtained from TLM measurements after acetic acid soaking. In contrast, the Paste B modules show much weaker darkening even after 1500 h of DH85 testing. The front Ag contacts remain electrically and mechanically intact, as reflected by the uniform EL brightness across the cells. Most cells maintained a stable EL intensity, indicating that electrical pathways and adhesion strength were preserved.

By correlating the module-level performance degradation with the microstructural and electrochemical analyses, a consistent conclusion can be drawn. The degradation behaviour suggests that the primary failure mechanism of the Paste A modules originates from the instability of the Pb/B-rich glass network. Under thermal and humidity stress, acetic acid generated inside the encapsulant gradually leaches Pb- and B-containing glass constituents, leading to the dissolution of the interfacial glass phase and the formation of voids between silver and the silicon surface. As

the interfacial conduction paths are disrupted, localized high-resistance regions develop, resulting in a macroscopic decline in both FF and P_{max}. However, in the metallization paste of Paste B modules, Ba^{2+} and Zn^{2+} were introduced as glass modifiers, facilitating the formation of a denser and chemically more durable glass network. In particular, the strong electrostatic field of Ba^{2+} enables the formation of robust ionic bonds with O^{2-}, thereby stabilizing the oxygen framework within the glass network and rendering it less susceptible to leaching under mildly acidic or humid conditions. The rear-side metallization exhibited stable performance at both the cell and module levels. In addition to the differences in paste formulation, this stability can also potentially be attributed to the distinct surface morphologies of the cell backsides. The polished surface is smoother and allows for tighter adhesion with the metal layer, effectively hindering the ingress of acid and moisture. These results demonstrate that the chemical stability of the glass frit is a decisive factor governing the long-term reliability of LAF-processed low-Al Ag paste TOPCon modules. Optimizing the glass frit composition represents an effective strategy to enhance metallization reliability for industrial TOPCon solar modules.

4 | Conclusion

This study systematically examined how the glass frit composition governs the corrosion and long-term reliability of LAF TOPCon solar cells and modules. Two commercial low-Al content Ag pastes were compared: Paste A with a Pb- and B-rich glass and Paste B containing Ba and Zn modifiers. Under identical fabrication and LAF conditions, both pastes initially enabled similar cell efficiencies (~25.2%), fill factors (~84.5%) and low contact resistivities (<2 m$\Omega\cdot$cm^2), indicating comparable as-fired contact quality.

Under accelerated acetic-acid exposure, the degradation pathways differed significantly. Paste A showed a rapid drop in efficiency of 80%–90% within 120 min, driven by a four-order-of-magnitude increase in R_s, whereas Paste B maintained stable electrical performance with only gradual losses. Microscopic analysis revealed severe interfacial delamination and glass dissolution in Paste A, whereas Paste B preserved a dense and adherent Ag/Si interface. The enhanced stability of Paste B is attributed to strong Ba–O ionic bonding, which suppresses proton-induced leaching, whereas Zn is likely to assist the formation of a more robust interfacial glass structure, although its effect depends on the overall frit composition.

These paste-dependent trends were mirrored at the module level. G–B TOPCon modules encapsulated with front EPE and rear EVA and metallised with Paste A suffered ~28%–30% power loss after 1500 h of DH85 testing, dominated by fill factor degradation and accompanied by pronounced EL darkening along the gridlines. In contrast, Paste B modules retained high stability, showing only 4%–5% relative power loss with uniform EL brightness and stable I_{sc} and V_{oc}.

Overall, these results demonstrate that the chemical durability of the glass frit rather than the metallic Ag phase governs metallization reliability in LAF TOPCon devices. Incorporating alkaline earth modifiers such as Ba and Zn into the glass network provides an effective means to mitigate acetic acid- and moisture-induced degradation, thereby enabling stable Ag–Si interfaces and extended module lifetimes. The direct cell-to-module correlation established here offers practical design guidelines for industrial metallization pastes and supports the deployment of cost-efficient, EVA-based G–B module configurations for next-generation TOPCon technologies.

Author Contributions

Jiexi Fu: writing – original draft, methodology, investigation, formal analysis. **Wei Wu:** investigation, formal analysis, data curation. **Yan Zhang:** methodology, investigation, formal analysis. **Lin Lv:** methodology, investigation, formal analysis. **Chao An:** resources, investigation, formal analysis. **Weiguang Yang:** investigation, formal analysis. **Zhan Wang:** investigation, formal analysis. **Jinshuai Song:** investigation, formal analysis. **Xutao Wang:** investigation, formal analysis, data curation. **Xinyuan Wu:** writing – review and editing, supervision, methodology, investigation, formal analysis, visualization, conceptualization. **Bram Hoex:** writing – review and editing, supervision, resources, project administration, methodology, funding acquisition, formal analysis, data curation.

Acknowledgements

This work was supported by the Australian Government through the Australian Renewable Energy Agency (ARENA) and the Australian Centre for Advanced Photovoltaics (ACAP). The Australian Government does not accept responsibility for the views, information or advice expressed herein. The authors gratefully acknowledge the Electron Microscope Unit (EMU) and the Inductively Coupled Plasma Laboratory (ICP Lab) at the University of New South Wales (UNSW) for access to characterization facilities, including the ZEISS cryogenic focused ion beam (Cryo-FIB) system. Special thanks are extended to Dr. Yin Yao and Dr. Charlie Kong for their technical assistance and to the Solar Industrial Research Facility (SIRF) team at UNSW for their continuous support. Jiexi Fu acknowledges the University International Postgraduate Award (UIPA) Scholarship from UNSW. During the preparation of this work, the authors used GPT-5.2 in order to improve the readability and language of the work. After using this tool, the authors reviewed and edited the content as needed and take full responsibility for the content of the publication. Open access publishing facilitated by University of New South Wales, as part of the Wiley - University of New South Wales agreement via the Council of Australasian University Librarians

Funding

This work was supported by the Australian Centre for Advanced Photovoltaics.

Data Availability Statement

The data that support the findings of this study are available from the corresponding author upon reasonable request.

References

1. Y. Zhou, D. Chen, Y. Ye, H. Yin, and X. Niu, "Damp-Heat Endurance Investigation of PV Modules Based on n-Type Bifacial Passivated Contact Cells," 40th Eur. Photovolt. Sol. Energy Conf. Exhib., 020210-001-020210-005, (2023), https://doi.org/10.4229/EUPVSEC2023/3AV.2.41.

2. Y. ChenLi, Z. Sun, D. Yan, et al., "Degradation Mechanism of TOPCon Solar Cells in an Ambient Acid Environment," *ACS Applied Materials & Interfaces* 17, no. 7 (2025): 10776–10783, https://doi.org/10.1021/acsami.4c21774.

3. C. Sen, H. Wang, M. U. Khan, et al., "Buyer Aware: Three New Failure Modes in TOPCon Modules Absent From PERC Technology," *Solar Energy Materials & Solar Cells* 272 (2024): 112877, https://doi.org/10.1016/j.solmat.2024.112877.

4. Y. Ye, Y. Zhou, Y. Wang, et al., "Damp-Heat Stability Investigation of Glass-Backsheet Modules Based on TOPCon Solar Cells," *Solar Energy Materials & Solar Cells* 292 (2025): 113764, https://doi.org/10.1016/j.solmat.2025.113764.

5. Y. Zeng, A. Gentle, R. Webster, et al., "Revisiting Photovoltaic Module Antireflection Coatings: A Novel, Dense Sol–Gel Design to Address Long-Standing Durability Limitations," *Progress in Photovoltaics: Research and Applications* 33, no. 12 (2025): 1400–1409, https://doi.org/10.1002/pip.3877.

6. X. Wu, C. Sen, X. Wang, et al., "Unveiling the Origin of Metal Contact Failures in TOPCon Solar Cells Through Accelerated Damp-Heat Testing," *Solar Energy Materials & Solar Cells* 278 (2024): 113188, https://doi.org/10.1016/j.solmat.2024.113188.

7. X. Wu, W. Wu, Y. Zhang, et al., "Is TOPCon Ready for EVA? Insights From Damp Heat Testing of Glass-Backsheet Modules," *Solar Energy Materials & Solar Cells* 288 (2025): 113650, https://doi.org/10.1016/j.solmat.2025.113650.

8. T. Fellmeth, H. Höffler, S. Mack, et al., "Laser-Enhanced Contact Optimization on iTOPCon Solar Cells," *Progress in Photovoltaics: Research and Applications* 30, no. 12 (2022): 1393–1399, https://doi.org/10.1002/pip.3598.

9. X. Wang, J. Yuan, X. Wu, et al., "Higher-Efficiency TOPCon Solar Cells in Mass Production Enabled by Laser-Assisted Firing: Advanced Loss Analysis and Near-Term Efficiency Potential," *Progress in Photovoltaics: Research and Applications* 33, no. 7 (2025): 771–781, https://doi.org/10.1002/pip.3921.

10. A. Mette, S. Hörnlein, F. Stenzel, et al., "Q.ANTUM NEO With LECO Exceeding 25.5% Cell Efficiency," *Solar Energy Materials & Solar Cells* 277 (2024): 113110, https://doi.org/10.1016/j.solmat.2024.113110.

11. X. Wu, X. Wang, W. Yang, et al., "Enhancing the Reliability of TOPCon Technology by Laser-Enhanced Contact Firing," *Solar Energy Materials & Solar Cells* 271 (2024): 112846, https://doi.org/10.1016/j.solmat.2024.112846.

12. F. J. Pern, "Ethylene-Vinyl Acetate (EVA) Encapsulants for Photovoltaic Modules: Degradation and Discoloration Mechanisms and Formulation Modifications for Improved Photostability," *Angewandte Makromolekulare Chemie* 252, no. 1 (1997): 195–216, https://doi.org/10.1002/apmc.1997.052520114.

13. M. C. Carvalho de Oliveira, A. S. Alves Cardoso Diniz, M. M. Viana, and V. D. Cunha Lins, "The Causes and Effects of Degradation of Encapsulant Ethylene Vinyl Acetate Copolymer (EVA) in Crystalline Silicon Photovoltaic Modules: A Review," *Renewable and Sustainable Energy Reviews* 81 (2018): 2299–2317, https://doi.org/10.1016/j.rser.2017.06.039.

14. N. Iqbal, M. Li, T. S. Sakthivel, et al., "Impact of Acetic Acid Exposure on Metal Contact Degradation of Different Crystalline Silicon Solar Cell Technologies," *Solar Energy Materials & Solar Cells* 250 (2023): 112089, https://doi.org/10.1016/j.solmat.2022.112089.

15. T. Tanahashi, N. Sakamoto, H. Shibata, and A. Masuda, "Corrosion Under Front Electrodes of Crystalline Silicon Photovoltaic Cells Predominantly Contributes to Their Performance Degradation," in *2019 IEEE 46th Photovoltaic Specialists Conference (PVSC)*, (IEEE, 2019), 2013–2016, https://doi.org/10.1109/PVSC40753.2019.8980636.

16. J. Irikawa, H. Hashimoto, H. Kanno, and M. Taguchi, "Correlation Between Damp-Heat Test and Field Operation for Electrode Corrosion in Photovoltaic Modules," *Solar Energy Materials & Solar Cells* 284 (2025): 113375, https://doi.org/10.1016/j.solmat.2024.113375.

17. M. D. Kempe, G. J. Jorgensen, T. J. McMahon, C. E. Kennedy, and T. T. Borek, *Potential Problems With Ethylene-Vinyl Acetate for Photovoltaic Packaging (Poster)* (National Renewable Energy Laboratory (NREL), 2006), https://www.osti.gov/biblio/893115.

18. S. Burgess and P. Pinard, "AZtec Wave—A New Way to Achieve Combined EDS and WDS Capability on SEM," *Microscopy and Microanalysis* 26, no. S2 (2020): 114–115, https://doi.org/10.1017/S1431927620013422.

19. "IEC 61215–2:2021," accessed December 14, 2025, https://webstore.iec.ch/en/publication/61350.

20. Y. Zhang, Y. Yang, J. Zheng, W. Hua, and G. Chen, "Thermal Properties of Glass Frit and Effects on Si Solar Cells," *Materials Chemistry and Physics* 114, no. 1 (2009): 319–322, https://doi.org/10.1016/j.matchemphys.2008.09.011.

21. C. Erdogan, M. Bengisu, and S. A. Erenturk, "Chemical Durability and Structural Analysis of PbO–B2O3 Glasses and Testing for Simulated Radioactive Wastes," *Journal of Nuclear Materials* 445, no. 1 (2014): 154–164, https://doi.org/10.1016/j.jnucmat.2013.10.025.

22. S. Kapoor, R. E. Youngman, K. Zakharchuk, A. Yaremchenko, N. J. Smith, and A. Goel, "Structural and Chemical Approach Toward Understanding the Aqueous Corrosion of Sodium Aluminoborate Glasses," *Journal of Physical Chemistry. B* 122, no. 48 (2018): 10913–10927, https://doi.org/10.1021/acs.jpcb.8b06155.

23. P. Trocellier, S. Djanarthany, J. Chêne, et al., "Chemical Durability of Alkali-Borosilicate Glasses Studied by Analytical SEM, IBA, Isotopic-Tracing and SIMS," *Nuclear Instruments and Methods in Physics Research Section B: Beam Interactions With Materials and Atoms* 240, no. 1 (2005): 337–344, https://doi.org/10.1016/j.nimb.2005.06.196.

24. H. Li, X. Sun, J. Xing, Y. Yang, X. Yuan, and H. Tong, "Effect of Glass Frit Composition on Reliability of Silver Paste Metallization in Crystalline Silicon Solar Cells," *Materials Research Express* 11, no. 5 (2024): 056303, https://doi.org/10.1088/2053-1591/ad48e4.

25. J. Zhang, X. Sun, H. Tong, Y. Yang, X. Yuan, and H. Li, "Mechanism Investigation on Effects of Glass Composition on Ag/Si Contact for Crystalline Silicon Solar Cells," *Journal of Materials Science: Materials in Electronics* 32, no. 6 (2021): 6778–6787, https://doi.org/10.1007/s10854-020-05211-8.

26. G. Ennas, A. Musinu, G. Piccaluga, A. Montenero, and G. Gnappi, "Structure and Chemical Durability of Zinc-Containing Glasses," *Journal of Non-Crystalline Solids* 125, no. 1 (1990): 181–185, https://doi.org/10.1016/0022-3093(90)90337-L.

27. Y. Chen, J. Li, Q. Jiang, A. Li, J. Yu, and H. Zeng, "Effect of Properties and Crystallization Behavior of BaO–ZnO–B2O3–SiO2 Glass on the Electrical Conductivity of Cu Paste," *Journal of the American Ceramic Society* 105, no. 9 (2022): 5687–5697, https://doi.org/10.1111/jace.18523.

28. W. Wu, K. E. Roelofs, S. Subramoney, K. Lloyd, and L. Zhang, "Role of Aluminum in Silver Paste Contact to Boron-Doped Silicon Emitters," *AIP Advances* 7, no. 1 (2017): 015306, https://doi.org/10.1063/1.4974752.

29. S. Kolay and P. Bhargava, "Role of MgO in Lowering Glass Transition Temperature and Increasing Hardness of Lithium Silicate Glass and Glass-Ceramics," *Ceramics International* 48, no. 9 (2022): 12699–12711, https://doi.org/10.1016/j.ceramint.2022.01.139.

30. S. Ibrahim and M. M. Morsi, "Effect of Increasing Fe2O3 Content on the Chemical Durability and Infrared Spectra of (25 − *x*) Na2O–*x* Fe2O3–25PbO–50SiO2 Glasses," *Materials Chemistry and Physics* 138, no. 2 (2013): 628–632, https://doi.org/10.1016/j.matchemphys.2012.12.030.

31. S. Wang, H. Liu, Y. Ao, K. Okamoto, and J. Di, "Strengthening TOPCon Solar Cell Reliability via Al/Ga/Fe-Added Glass Frits in LECO-Compatible Silver Pastes Against Acid Corrosion," *Solar Energy Materials & Solar Cells* 292 (2025): 113776, https://doi.org/10.1016/j.solmat.2025.113776.

32. Microscopy Australia, "Scanning Electron Microscopy (SEM)—Spectroscopy," accessed October 30, 2025, Technique Finder, https://micro.org.au/techniquefinder/Portal/viewTechnique/52.

33. J. S. Luo, S. F. Wolf, W. L. Ebert, and J. K. Bates, "SEM/EDS Analysis of Boron in Waste Glasses With Ultrathin Window Detector and Digital Pulse Processor," (1996), 30. annual meeting of Microbeam Analysis Society, Minneapolis, MN (United States), https://digital.library.unt.edu/ark:/67531/metadc671365/.

34. B. J. A. Moulton, L. D. Silva, C. Doerenkamp, et al., "Speciation and Polymerization in a Barium Silicate Glass: Evidence From 29Si NMR and Raman Spectroscopies," *Chemical Geology* 586 (2021): 120611, https://doi.org/10.1016/j.chemgeo.2021.120611.

35. P. Zhao, S. Kroeker, and J. F. Stebbins, "Non-Bridging Oxygen Sites in Barium Borosilicate Glasses: Results From 11B and 17O NMR," *Journal of Non-Crystalline Solids* 276, no. 1 (2000): 122–131, https://doi.org/10.1016/S0022-3093(00)00290-8.

36. D. A. Aloraini, A. Almuqrin, B. Albarzan, E. A. A. Wahab, and K. S. Shaaban, "Synthesis, Structural, Mechanical, Thermal, and Radiation Shielding Characterization of Aluminum Borosilicate Glasses Containing BaO and ZnO Oxides," *European Physical Journal Plus* 140, no. 8 (2025): 724, https://doi.org/10.1140/epjp/s13360-025-06680-8.

37. P. Sahu and S. M. Ali, "BaO-Doped Silicate and Borosilicate Glasses for Enhanced Chemical Durability: Molecular Dynamics Simulations Based Strategy for Glass Design," *Molecular Systems Design and Engineering* 7, no. 11 (2022): 1477–1500, https://doi.org/10.1039/D2ME00094F.

38. J. D. Fields, M. I. Ahmad, V. L. Pool, et al., "The Formation Mechanism for Printed Silver-Contacts for Silicon Solar Cells," *Nature Communications* 7 (2016): 11143, https://doi.org/10.1038/ncomms11143.

39. J. Liu, Z. Guo, Y. Fu, Y. Sun, Q. Li, and S. Ma, "Effect of Wettability and Thermal Properties of Glass Frits on the Interconnection Reliability of Solar Cell Busbars," *Journal of Alloys and Compounds* 1014 (2025): 178665, https://doi.org/10.1016/j.jallcom.2025.178665.

40. F. He, J. Wang, and D. Deng, "Effect of Bi2O3 on Structure and Wetting Studies of Bi2O3–ZnO–B2O3 Glasses," *Journal of Alloys and Compounds* 509, no. 21 (2011): 6332–6336, https://doi.org/10.1016/j.jallcom.2011.03.087.

41. J. Liu, X. Xu, T. Zheng, Y. Guo, and J. Lv, "Effect of Bi2O3 Content on the Structure and Properties of Bi2O3-B2O3-BaO-ZnO Glass," *Journal of Non-Crystalline Solids* 575 (2022): 121211, https://doi.org/10.1016/j.jnoncrysol.2021.121211.

42. E. A. Mahdy, S. Ibrahim, and H. A. Abo-Mosallam, "The Influence of Bi2O3 on Structural and Enhancing Physical Properties of Li2O–Fe2O3–In2O3–P2O5 Glasses," *Materials Chemistry and Physics* 309 (2023): 128406, https://doi.org/10.1016/j.matchemphys.2023.128406.

43. H. A. Saudy, S. E. Mosallamy, S. U. E. Kameesy, N. Sheta, A. G. Mostafa, and H. A. Sallam, "Mechanical, Thermal and Chemical Durability Behaviors of CdO-Bi2O3 Boro-Phosphate Glasses Containing Fe2O3," *World Journal of Condensed Matter Physics* 3, no. 1 (2013): 9–13, https://doi.org/10.4236/wjcmp.2013.31002.

Supporting Information

Additional supporting information can be found online in the Supporting Information section. **Table S1:** The initial I-V data of the experimental TOPCon solar cells made by Pastes A and B. **Table S2:** Raw data from ICP-MS for the analysis of Pastes A and B. **Figure S1:** Cross-sectional EDS point ID locations (orange dots). **Figure S2:** The initial cross-sectional EDS mapping of Paste A and Paste B samples.